

Borehole seismoelectric logging using a shear-wave source: Possible application to CO₂ disposal?



Fabio I. Zyserman^{a,*}, Laurence Jouniaux^b, Sheldon Warden^b, Stéphane Garambois^c

^a CONICET, and Facultad de Ciencias Astronómicas y Geofísicas, Universidad Nacional de La Plata Paseo del Bosque s/n, 1900 La Plata, Argentina

^b Institut de Physique du Globe de Strasbourg, Uds-CNRS UMR 7516, Université de Strasbourg, 5 rue René Descartes, 67084 Strasbourg, France

^c ISTerre, Université Grenoble Alpes, CNRS UMR 5275, Grenoble, France

ARTICLE INFO

Article history:

Received 6 April 2014

Received in revised form 2 December 2014

Accepted 8 December 2014

Keywords:

Seismoelectrics

Seismomagnetism

Partial CO₂ saturation

ABSTRACT

The behaviour of CO₂ deposition sites – and their surroundings – during and after carbon dioxide injection has been matter of study for several years, and several geophysical prospecting techniques like surface and crosshole seismics, geoelectrics, controlled source electromagnetics among others, have been applied to characterize the behaviour of the gas in the reservoirs. Until now, Seismoelectromagnetic wave conversions occurring in poroelastic media via electrokinetic coupling have not been tested for this purpose. In this work, by means of numerical experiments using Pride's equations – extended to deal with partial saturations – we show that the seismoelectric and seismomagnetic interface responses (IR) generated at boundaries of a layer containing carbon dioxide are sensitive to its CO₂ content. Further, modeling shear wave sources in surface to borehole seismoelectric layouts and employing two different models for the saturation dependence of the electrokinetic coefficient, we observe that the IR are sensitive to CO₂ saturations ranging between 10% and 90%, and that the CO₂ saturation at which the IR maxima are reached depends on the aforementioned models. Moreover, the IR are still sensitive to different CO₂ saturations for a sealed CO₂ reservoir covered by a clay layer. These results, which should be complemented by the analysis of the IR absolute amplitude, could lead, once confirmed on the field, to a new monitoring tool complementing existing ones.

© 2014 Elsevier Ltd. All rights reserved.

1. Introduction

Injection of large amounts of man-produced CO₂ in depleted oil wells below the sea floor and in other appropriate geological formations has been used, for several years, as a means of reducing the carbon dioxide emissions into the atmosphere. For example, CO₂ is being injected in the Sleipner field in the North Sea since 1996 at a rate of 0.85 Mt per year (Ellis, 2010), and also beneath the Sahara desert, at In Salah in Algeria (Ringrose et al., 2009). The former has been a subject of extensive theoretical and experimental studies, including laboratory rock sample analysis, seismic monitoring, etc. We mention, from the large literature concerning this deposition site, the studies of Chadwick et al. (2009, 2010) where time-lapse seismic is employed to characterize CO₂ plume development, and the studies of Gomez and Ravazzoli (2011), where CO₂ content related to seismic attributes were investigated. Moreover, a test site in Ketzin, Germany, is being run and extensively studied

in order to monitor the CO₂ behaviour during and after injection, see Martens et al. (2012, 2013) and references therein. Scientists from different areas have been studying this topic, and a still open problem is to predict the behaviour of the gas once set into the reservoir. Will it remain stable? Will it migrate, and make its way back to the surface? How the stored CO₂ can be efficiently monitored in order to avoid pollution of overlying aquifers by leaked gas, among other issues (Thibeau and Mucha, 2011) is still a topic of intense research.

Among other works implemented at Ketzin, Wiese et al. (2010) studied the hydraulic properties of the storage reservoir, Kazemeini et al. (2010) carried out some rock physics and seismic modeling studies of surface seismic CO₂ monitoring, and cross-well seismic tomography has been also performed (Zhang et al., 2012); more recently Fischer et al. (2013) made laboratory studies of geochemical changes induced in Ketzin rock matrix samples by the presence of the stored carbon dioxide, and Wiese et al. (2013) studied – at the same site – not only the geochemical but also the hydraulic changes induced in the overburden by deposited CO₂. We can also mention that both seismic and electric methods are potentially appropriate to study the CO₂ reservoir (Fabriol

* Corresponding author. Tel.: +542214236593x137; fax: +54 2214236591.
E-mail address: zyserman@fcaglp.unlp.edu.ar (F.I. Zyserman).

et al., 2011; Girard et al., 2011; Carcione et al., 2012). Martens et al. (2012) describe not only the results of different campaigns including seismic, surface and borehole monitoring, but also some seismic simulation runs in order to check previous models; on the other hand synthetic and field geoelectrical methods were applied to study possible gas migration (Kiesling et al., 2010). Moreover Ishido et al. (2013) have numerically investigated the application of self potential methods to monitor the migration of CO₂ sequestered into saline aquifers, concluding that the used methods are effective for sensing the approach of CO₂ to the well casings deep within the subsurface. We finally point out that in recent studies it was shown that seismics was useful to detect CO₂ saturation below 15% and that electrical resistivity was useful to detect CO₂ saturation above 15% (Kim et al., 2013).

Seismoelectric signals are electrokinetically generated by the propagation of seismic waves within a porous material. They can be recorded using a seismic source and electric receivers. The seismoelectric strategy aims to combine the resolution of the seismics to the sensitivity of the electric methods to fluid content. A specific seismoelectric signal, denoted the interfacial response, is expected to be induced at contrasts between rock properties (Garambois and Dietrich, 2002), including different fluids and different fluid-contents. This signal is usually weak compared to the so-called coseismic signal, which is the seismo-electric signal travelling within the seismic wave directly induced by the source. Several authors have investigated the benefits of surface-to-borehole seismoelectric layouts to accomplish efficient measurements of the interfacial response, as opposed to layouts for which both the seismic source and the receiving electrodes are laid at the surface.

The aim of this work is to provide numerical evidence that borehole seismoelectrics can discern carbon dioxide concentrations in a broader range than seismics allow, detecting at the same time salinity contrasts, task up to now fulfilled by geoelectrics. The pure SH seismic source considered in the present study could achieve a better resolution than the one obtained through the usual P-driven experiments because of shorter wavelengths.

We start our work by reviewing the most important theoretical concepts of seismoelectrics, and by proposing a possible appropriate field experimental setup. We follow by analyzing shear-wave driven interface responses generated between two consecutive units saturated with water, using a one dimensional finite element method to approximate the solution to Pride's equations. We study the sensitivity of these responses to contrasts in relevant parameters, such as porosity, salinity and viscosity; and continue by investigating the coseismic waves and interface response amplitudes of tabular media when one layer is partially saturated with carbon dioxide, employing in this analysis different models to take into account this situation in the electrokinetic coupling. Finally, we consider a layered model including a seal layer, in order to simulate a realistic CO₂ deposition site.

2. Theoretical background

The seismoelectric method relies on electrokinetically induced seismic-to-electric energy conversions occurring in fluid-containing porous media. The reader can find a tutorial on electrokinetics in Jouniaux and Ishido (2012).

2.1. Theoretical aspects

When a compressional wave travels through a porous medium, it creates a fluid-pressure gradient and an acceleration of the solid matrix, inducing a relative motion between the ions adsorbed at the grain surface and the counter-ions in the diffuse layer. This charge separation at the scale of the seismic wavelet creates an electrical

potential difference known as the streaming potential. The electric field arising from this potential is known as the coseismic wave, as it travels within the passing compressional seismic waves. Therefore coseismic electric fields do not extend outside the seismic waves creating them, and may only help characterize the medium near the receivers. For borehole seismoelectric measurements they give information about the medium in the vicinity of the well (Mikhailov et al., 2000).

Another type of seismoelectric conversions arises when a seismic wave crosses a contrast between mechanical or electrical properties (Haartsen and Pride, 1997; Chen and Mu, 2005; Block and Harris, 2006). In this situation a transient localized charge separation across the interface is created, which acts as a secondary source that can be approximated as an electrical dipole oscillating at the center of the first Fresnel zone (Thompson and Gist, 1993; Garambois and Dietrich, 2002). The resulting electromagnetic (EM) wave is known as the interface response (IR), and diffuses independently from the seismic wavefield: the velocity at which it travels is several orders of magnitude greater than seismic velocities. This IR may provide information about the contrasts in the medium's properties at depth.

The equations governing the coupled seismic and electromagnetic wave propagation in fluid-filled porous media were derived by Pride (1994) by combining Maxwell's equations with Biot's equations for poroelasticity (Biot, 1956a,b). Two coupled transport equations were derived (Eq. 251 and 252 in Pride (1994)):

$$\mathbf{J} = \sigma(\omega)\mathbf{E} + L(\omega)(-\nabla p + \omega^2 \rho_w \mathbf{u}_s) \quad (1)$$

$$-i\omega \mathbf{u}_f = L(\omega)\mathbf{E} + \frac{k(\omega)}{\eta_w}(-\nabla p + \omega^2 \rho_w \mathbf{u}_s) \quad (2)$$

The macroscopic electrical current density \mathbf{J} [A/m²] is given in Eq. (1) as the sum of the average conduction and streaming current densities, respectively the first and second term of its right-hand side. Both the above equations assume a $e^{-i\omega t}$ time dependence of the propagating wave, where ω [rad/s] denotes the angular frequency. The parameter \mathbf{E} [V/m] denotes the electric field and $\sigma(\omega)$ [S/m] is the frequency-dependent conductivity of the material. Streaming currents may be induced by both the pressure gradient $-\nabla p$, where p [Pa] is the pore-fluid pressure, and the acceleration of the solid frame $\omega^2 \rho_w \mathbf{u}_s$, where ρ_w [kg/m³] is the density of the fluid (water) and \mathbf{u}_s [m] denotes the solid displacement. The fluid velocity $-i\omega \mathbf{u}_f$ [m/s] is written in Eq. (2) as the sum of electrically and mechanically induced contributions. The frequency-dependent permeability is written as $k(\omega)$ [m²] and the dynamic viscosity of the fluid is expressed as η_w [Pa s]. The complex and frequency-dependent coupling $L(\omega)$ links Eqs. (1) and (2):

$$L(\omega) = L_0 \left[1 - i \frac{\omega}{\omega_t} \frac{b}{4} \left(1 - 2 \frac{d}{\Lambda} \right)^2 \left(1 - i^{3/2} d \sqrt{\frac{\omega \rho_w}{\eta_w}} \right)^2 \right]^{-1/2} \quad (3)$$

In Eq. (3), Λ [m] is a pore geometrical parameter, defined in Johnson et al. (1987), whereas b is a dimensionless parameter defined in terms of the latter, the porosity ϕ , the absolute permeability k_0 and the tortuosity α_∞ as $b = (\phi/\alpha_\infty k_0)\Lambda^2$ and consisting only of the pore-space geometry terms. This parameter b was originally denoted m in Pride (1994). When k_0 , ϕ , α_∞ and Λ are independently measured, b is comprised between 4 and 8 for a variety of porous media ranging from grain packing to capillary networks consisting of tubes of variable radii (Johnson et al., 1987). The parameter d [m] denotes the Debye length, while ω_t [rad/s] is the permeability-dependent transition angular frequency between the low-frequency viscous flow and high-frequency inertial flow. Finally, L_0 denotes the electrokinetic coupling which expression we give below. The coupling $L(\omega)$ was studied by Reppert et al. (2001), Schoemaker et al. (2007), Jouniaux and Bordes (2012) and Glover et al. (2012). When this

coefficient is set to zero, the two subsets of equations describing the behavior of EM and seismic waves are decoupled. Different modellings have been developed to resolve the seismoelectric conversions, see for example (Guan et al., 2013; Schakel et al., 2012, 2011; Gao and Hu, 2010; Guan and Hu, 2008).

2.2. Transfer functions

The displacement and EM fields in an isotropic and homogeneous whole space were derived by Pride and Haartsen (1996) using a plane-wave solution of the governing equations. Later, Garambois and Dietrich (2001) making use of these results, derived the electric and magnetic fields \mathbf{E} and \mathbf{H} as a function of the seismic displacement \mathbf{u} . They demonstrated that low-frequency approximations of these relationships lead to a seismoelectric field \mathbf{E} proportional to the grain acceleration $\ddot{\mathbf{u}}$ associated to longitudinal fast P -waves as:

$$\mathbf{E} \simeq \frac{\epsilon_0 \kappa_w \zeta}{\eta_w \sigma_w} \rho_w \left(1 - \frac{\rho}{\rho_w} \frac{C}{H}\right) \ddot{\mathbf{u}} = C_K \rho_w \left(1 - \frac{\rho}{\rho_w} \frac{C}{H}\right) \ddot{\mathbf{u}}; \quad (4)$$

moreover, Garambois and Dietrich (2001) verified the consistency of this relation on real field P -wave volume waves. The definitions of the C and H moduli are those of Biot (1962); ϵ_0 is the vacuum permittivity, κ_w and σ_w are the dimensionless dielectric constant and the electrical conductivity of the saturating fluid respectively. The zeta potential ζ [V] is the electric potential on the slipping plane within the electric double layer.

Therefore the coseismic electric field is also proportional to the electrokinetic coefficient C_K largely studied in laboratory and modeled (Vinogradov and Jackson, 2011; Vinogradov et al., 2010; Aizawa et al., 2008; Guichet et al., 2006; Mainault et al., 2006; Jouniaux et al., 1999, 1994; Pozzi and Jouniaux, 1994; Ishido and Mizutani, 1981).

The magnetic field \mathbf{H} has been shown to be proportional to the velocity $\dot{\mathbf{u}}$ associated to transverse SH - and SV -waves as:

$$|\mathbf{H}| \simeq \frac{\phi}{\alpha_\infty} \frac{\epsilon_0 \kappa_w |\zeta|}{\eta_w} \rho_w \sqrt{\frac{G}{\rho}} |\dot{\mathbf{u}}| \quad (5)$$

where G is the shear modulus of the framework. The tortuosity α_∞ is usually taken equal to the product of the porosity by the formation factor F . The magnetic field can also be expressed as a function of the electrokinetic coefficient C_K as:

$$|\mathbf{H}| \simeq \frac{\epsilon_0 \kappa_w |\zeta|}{\eta_w \sigma_w} \frac{\sigma_w}{F} \rho_w \sqrt{\frac{G}{\rho}} |\dot{\mathbf{u}}| = C_K \frac{\sigma_w}{F} \rho_w \sqrt{\frac{G}{\rho}} |\dot{\mathbf{u}}| \quad (6)$$

Therefore the coseismic magnetic field is also proportional to the electrokinetic coefficient, considering that the water density and conductivity are constant, as are the formation factor and the G , C , H moduli.

3. Appropriate field experimental setup

Although performing a field experiment is beyond the scope of this paper, we would like to emphasize what would be the most appropriate geometry to be developed to detect seismoelectromagnetic conversions for CO_2 disposal monitoring. The interfacial response can provide information about the formations at depth while the co-seismic signal provides only information of the soil in the vicinity of the electrodes. The challenge is therefore to isolate the interfacial response, which is often of the order of 1–100 $\mu\text{V}/\text{m}$ (Mikhailov et al., 2000; Chen and Mu, 2005; Liu et al., 2008).

3.1. Signal processing

The first step in processing the seismoelectric data is to remove the noise from power lines, which can be of the order of 1 mV/m. The estimate of the harmonic noise can be performed on the data recorded just before the shot, using a pre-trigger recording. The filtering of this noise can be performed by applying a single frequency adaptive noise cancellation filter. Butler et al. (1996) proposed to apply the techniques of block and sinusoidal subtraction. Presently the most efficient method which is used for most of the observations is to routinely reduce the harmonic noise using the algorithm of Butler et al. (1996), Butler and Russell (2003), Butler et al. (2007) applied to individual shots before the stacking. Wiener and bandpass filters can be used to reduce high-frequency noise. Supplementary techniques as delay-line filtering in case of severe noise, and low-pass filtering in case of strong high-frequency noise contamination can be used.

3.2. Benefit of surface-to-borehole measurements

The main issue for detecting the weak IR signal is often the high amplitude of the co-seismic signal. We propose to perform the electromagnetic measurements in borehole so that this IR signal can be recorded before the arriving of the co-seismic signal. Indeed the interfacial response can be observed free from the coseismic signal when the electrodes are located below the interface of interest (Dupuis et al., 2007), by measuring the electric field within a borehole. In (Haines, 2004; Haines et al., 2007) field experiments were conducted in which the source and the receivers were laid on opposite sides of one or two man-made sand-filled trenches dug in a clayey background. This fan-shape layout enabled the measurement of the Interface Response as it reached the electric receivers before the typically stronger Coseismic wavefield. Therefore, the authors suggested that by setting the source at the surface and the electrodes in a borehole below the interfaces of interest, one may separate the different types of seismoelectric waves without resorting to numerical wave separation techniques. This layout-related separation may better preserve the amplitudes and waveforms of seismoelectric signals than numerical data processing such as $f-k$ or $\tau-p$ filtering, often distorting seismoelectric signals (Warden et al., 2012). Moreover, with this layout the influence of surface waves is strongly decreased; however Stoneley waves may appear; which should be dealt with.

Another benefit of surface-to-borehole geometries is related to the amplitudes of the Interface Response. When working with surface geometries, deep interfaces become rather harder to track as the amplitudes of the associated interfacial signals may have decayed below the noise level by the time they reach the surface. Setting the receivers close to the target interfaces therefore allows to pick up stronger signals (Haines and Pride, 2006). Furthermore, when working with uncased wells (Zhu et al., 1999), deploying the receivers at depth also allows to take advantage of the Coseismic signal, which provides information about the subsurface in the vicinity of the receivers (Garambois and Dietrich, 2001; Haines et al., 2007; Bordes et al., 2008). For instance, by hitting the upper casing of a borehole with a sledgehammer, Mikhailov et al. (2000) triggered Stoneley waves, which in turn induced a pore fluid flow in the permeable zones intersecting the borehole. The authors were able to measure the small (tens of microvolts) electrical signals associated with this flow.

3.3. Seismic source

We propose to use a pure SH seismic source that could achieve a better resolution than the one obtained through the usual P -driven experiments because of shorter wavelengths. As stated in Haines

and Pride (2006), there is no coseismic electric field for S-waves, but the coseismic magnetic field is present; therefore the electric IR may be easier to be detected than the magnetic IR.

In the next sections, we use a 120 Hz peak frequency for the source to keep the response in time fairly sharp, so that the different events could be easily resolved. But, as for the whole range of seismic frequencies both the dynamic permeability and the electrokinetic coupling coefficient are almost independent of the frequency, qualitatively the same responses would be obtained for a source with peak frequency of 40 Hz or 60 Hz. A pure shear wave source is difficult to achieve; however surface vibrators for SH-source do exist, which can emit SH-waves as well as SV-waves, being designed for a peak force of approximately 30 kN (equivalent to the free fall of a 3 t mass from a height of 1 m) and a frequency range of 16–300 Hz.

Furthermore, there is presently interest in the seismics community in S-wave exploration because of its application in unconventional reservoirs; an application in heavy oil production management through S-wave data monitoring of stress effects in the reservoir has been reported (Bale et al., 2013), as well as monitoring of the seal of a CO₂ deposition site (Davis et al., 2013). This situation could contribute to facilitate further progress in field measurements in seismoelectrics using shear wave sources.

4. Modeling seismoelectric and seismomagnetic signals measured at depth using a shear-wave source

In this section we use a numerical simulator, which features infinite shear sources generating 1D wave fields in likewise layered media for the modeling of the seismoelectric conversions; see the appendix for details in the 1D SHTE formulation. We model the seismoelectric and seismomagnetic conversions induced by a shear-wave source within a tabular model consisting of a sand layer over a sandstone layer. We then describe the results of the horizontal displacement, the horizontal electric field, and the horizontal magnetic field as a function of depth for full water saturation conditions.

4.1. Model description

We consider a simple tabular model consisting of a sand layer, 30.5 m thick, set on top of a sandstone half-space (Fig. 1).

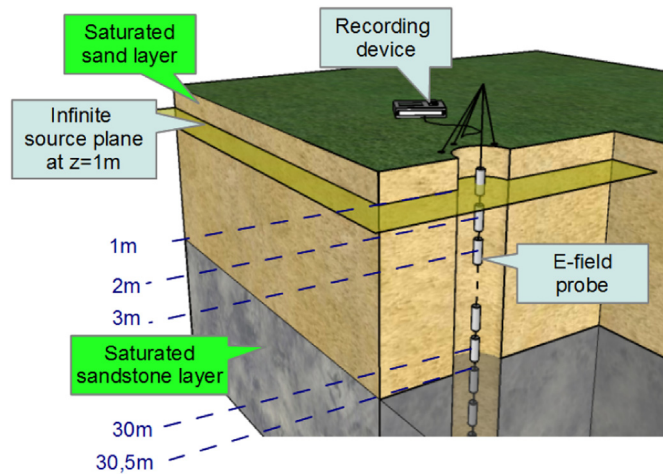


Fig. 1. Tabular model and seismoelectric vertical profiling layout. The subsurface consists of a fully saturated 30.5 m thick sandstone layer on top of a saturated sand half-space. The source is oriented along y, 51 dipole receivers – set 1 m apart – are deployed inside a vertical uncased borehole.

Table 1

First two columns correspond to properties of the model described in Section 4.1, whilst the third one to the model used in Section 5. Seismic and electromagnetic velocities are calculated at the source peak frequency of 120 Hz.

	Sand	Sandstone I	Sandstone II
ϕ (%)	35	20	12
m	2.05	1.7	1.7
k_0 (m ²)	10^{-11}	10^{-13}	4.32×10^{-13}
k_s (Pa)	36×10^9	36×10^9	36×10^9
k_f (Pa)	2.27×10^9	2.27×10^9	2.27×10^9
k_{fr} (Pa)	2.92×10^9	14.40×10^9	18.45×10^9
G_{fr} (Pa)	2.49×10^9	14.08×10^9	20.38×10^9
v_s (m/s)	1104	2485	2909
v_p (m/s)	2344	4017	4529
v_{EM} (m/s)	8.69×10^5	1.03×10^6	3.1×10^6
η_w (Pa s)	1×10^{-3}	1×10^{-3}	1×10^{-3}
η_g (Pa s)	1.8×10^{-5}	1.8×10^{-5}	1.8×10^{-5}
ρ_s (kg/m ³)	2.6×10^3	2.6×10^3	2.6×10^3
ρ_w (kg/m ³)	1×10^3	1×10^3	1×10^3
ρ_g (kg/m ³)	1	1	1
C_0 (mol/L)	1×10^{-3}	1×10^{-3}	1×10^{-3}
σ (S/m)	1.59×10^{-3}	1.14×10^{-3}	1.2×10^{-4}
ζ (V)	-0.07	-0.07	-0.07
κ_w	80	80	80
κ_s	4	4	4
κ_g	1	1	1
T (K)	298	298	298

We model a seismic transverse source of peak frequency $f_{peak}=120$ Hz at a depth of $z_s=1$ m, the source wavelet being a Ricker wavelet, or “Mexican hat” wavelet, which generates seismoelectric signals recorded by a vertical array located right under the source; this array consists of 51 seismic and electromagnetic transverse receivers, evenly spaced between a depth of 1 and 51 m so that there are receivers on either side of the interface.

The considered source is a shearing force per unit volume applied along y on a whole horizontal plane located at the source depth with the already described signature, its implementation can be seen in the appendix.

Both sand layer and sandstone layer – called Sand and Sandstone I in Table 1, where their properties are detailed – are fully saturated with a moderately briny water ($C_0=10^{-3}$ mol/L). As there is no salinity contrast between the two layers and since we compute the ζ potential as $\zeta=0.008+0.026 \log_{10}(C_0)$ (Pride and Morgan, 1991), $\zeta=-70$ mV throughout the entire model. The frame bulk modulus K_{fr} [Pa] is deduced from the solid bulk modulus K_s [Pa], following Pride (2005) and assuming a consolidation parameter of 20 for sand and 5 for sandstone as

$$K_{fr} = K_s \frac{1 - \phi}{1 + c_s \phi}. \quad (7)$$

The frame shear modulus G_{fr} [Pa] is linked to the solid shear modulus modulus G_s in a similar fashion:

$$G_{fr} = G_s \frac{1 - \phi}{1 + 1.5c_s \phi}. \quad (8)$$

As we deal in next sections with porous media saturated with mixtures of water and CO₂, it is necessary to introduce appropriate effective properties in order to use them within Pride’s formulation for electroseismics. Therefore, for the effective fluid mass density we use

$$\rho_f = \rho_w S_w + \rho_{CO_2} (1 - S_w), \quad (9)$$

where $S_w + S_{CO_2} = 1$ is assumed and subscripts CO₂ and w refer to carbon dioxide and water respectively, S_w denotes water saturation. For the effective bulk modulus of such fluid mixture we use Brie et al. (1995) approach

$$K_f = (K_w - K_{CO_2}) S_w^5 + K_{CO_2}; \quad (10)$$

the power five in this expression is chosen following Carcione et al. (2006). Here the CO₂ is supercritical as explained in Section 6 and there is no gaseous phase in our model. The effective viscosity is computed in terms of the mixture components viscosities η_l , $l = w, \text{CO}_2$ and water saturation S_w using Teja and Rice (1981)

$$\eta_f = \eta_{\text{CO}_2} \left(\frac{\eta_w}{\eta_{\text{CO}_2}} \right)^{S_w} \quad (11)$$

In order to characterize the electric conductivity of the effective fluid saturated solid matrix we use the expression recently proposed by Warden et al. (2013), extending Pride's original formula (Pride, 1994, Eq. (242)) to the realm of partially saturated media:

$$\sigma(S_w, \omega) = \frac{S_w^n}{F} \sigma_w + \frac{2}{F} \frac{C_{em} + C_{os}(\omega)}{\Lambda} \quad (12)$$

The first term in this equation – where $F = \phi^{-m}$ stands for the formation factor, m being the cementation coefficient – is Archie's law for a partially saturated medium, while the second term accounts for the surface conductivity. In the latter, – as Pride stated in his liminar work– the factor C_{em} [S] is the excess conductance associated with the electromigration of double layer ions; $C_{os}(\omega)$ [S] is the frequency-dependent electro-osmotic conductance due to electrically induced streaming of the excess double-layer ions and Λ [m] is the above presented pore-geometry dependent factor. We remark here that, as in Brovelli et al. (2005) and Warden et al. (2013), the surface conductivity is assumed to be independent of water saturation S_w , because under realistic saturation ranges (residual water saturation $S_{wr} \geq 10\%$) the thickness of the wetting phase layer on the pore surface is always larger than the Debye length d . This also means that all fluid related properties involved in the calculation of the surface conductivity and of the electrokinetic coupling – see below – are just those of water.

Again, following Warden et al. (2013), we propose for the effective fluid saturated media the following electrokinetic coupling:

$$L_0(S_w) = - \frac{\phi}{\alpha_\infty} \frac{\epsilon_0 \kappa_w \zeta}{\eta_w} \left(1 - 2 \frac{d}{\Lambda} \right) S_w^n S(S_w), \quad (13)$$

In this equation n is Archie's saturation exponent (taken to be equal to the cementation exponent) and $S(S_w)$ is a function relating the streaming potential coefficient obtained under partial saturation conditions to the one corresponding to full saturation conditions. Several authors investigated this relation from both theoretical and experimental viewpoints; Perrier and Morat (2000), Guichet et al. (2003), Revil et al. (2007), and Strahser et al. (2011) predict a monotonic behaviour with saturation, Jackson (2010) suggested that the coupling coefficient could be either monotonic or non-monotonic depending on the properties of the saturating phases, while Allègre et al. (2010) and Allègre et al. (2012) observed and modeled a non-monotonic behaviour while studying laboratory drainage experiments; we select for the present work two expressions for $S(S_w)$ displaying a qualitatively distinct behaviour, meaning monotonic and non-monotonic:

$$S(S_w) = \begin{cases} \frac{1}{S_w^n} \left(\frac{S_w - S_{wr}}{1 - S_{wr}} \right)^2 & S_{wr} = 0.10 \quad (\text{Perrier and Morat, 2000}) \\ \left(\frac{S_w - S_{wr}}{1 - S_{wr}} \right) \left(1 + 32 \left(1 - \left(\frac{S_w - S_{wr}}{1 - S_{wr}} \right) \right)^{0.4} \right) & S_{wr} = 0.305 \quad (\text{Allègre et al., 2010}). \end{cases} \quad (14)$$

4.2. Seismic and seismo-electromagnetic results

In this section we present our first results; here it should be noticed that they correspond to media saturated with water, i.e. $S_{\text{CO}_2} = 0$, and that free surface reflections are neglected.

On the synthetic recording displaying the horizontal solid displacement (Fig. 2(a)), one can notice the downgoing direct S-wave

$u_{y,i}$, traveling at $v_S = 1104$ m/s. When this direct wave hits the interface located at 30.5 m depth at about 0.027 s, part of the total incident energy reflects back to the surface as an upgoing S wave $u_{y,r}$ with the same velocity as the incident wave. The transmitted downgoing S wave $u_{y,t}$ travels at a higher velocity of $v_S = 2485$ m/s.

On the synthetic recording displaying the horizontal electric field (Fig. 2(b)), one can distinguish three events. An event with zero moveout –labeled as E_D in this figure– appears at the time at which the source is triggered (0.01 s). This flat arrival may be related to the direct field predicted by Pride and Haartsen (1996) and measured by Haines (2004).

An event we associate with a first Interface Response – E_{IR} in the figure – arises at about 0.027 s, that is, at about the time needed for the S-wave to reach the interface. A second Interface Response E_{IR2} occurring at the surface when the S-wave reflected at the 30.5 m deep interface $u_{y,r}$ reaches the surface, is seen at two-way travel-time. Its origin could be partially due to a numerical artifact caused by the boundary conditions for Biot equations at the Earth surface; further modelling with independent codes and field experiments will help clarify this question.

It is also interesting to notice that, as stated in Haines and Pride (2006), there is no coseismic electric field for S-waves, but the coseismic magnetic field is present, as can be seen in Fig. 2(c). The magnetic field existing within the seismic shear wave travels at the same velocity as the latter: the incident coseismic magnetic field $H_{C,i}$ arrives at the 30.5 m depth interface at about 0.027 s, and is partially transmitted – see $H_{C,t}$ in the figure – and partially reflected towards the surface as $H_{C,r}$. It is also possible to see the flat event associated to the direct field H_D , at about 0.01 s, and a first Interface Response H_{IR} generated simultaneously with the arrival of the seismic wave to the interface. The amplitude of the Interface Response is negligible in the upper layer. Finally, the second Interface Response occurring at the Earth surface, labeled H_{IR2} in the figure, is also present for the magnetic field.

5. Sensitivity of the interface response to contrasts in fluid and rock properties

In this section we describe the amplitude of the interfacial response induced by a S-wave source when some physical properties of the sandstone half-space are changed whereas an upper sandstone layer is kept with constant parameters. The properties of the upper sandstone layer (Sandstone II) are given in the third column of Table 1.

5.1. Porosity contrast

In this paragraph we study the influence of a porosity contrast on the amplitude of the interfacial response. The porosity in the lower half-space is allowed to change between 2 and 24%. The empirical relation of Bourbié et al. (1987) linking porosity and permeability

in Fontainebleau sandstones is used to account for the influence of porosity changes on permeability,

$$k_0 = 1.66 \times 10^{-4} \phi^8 \quad \text{for } \phi < 6\% \quad (15)$$

$$k_0 = 2.5 \times 10^{-10} \phi^3 \quad \text{for } \phi > 6\% \quad (16)$$

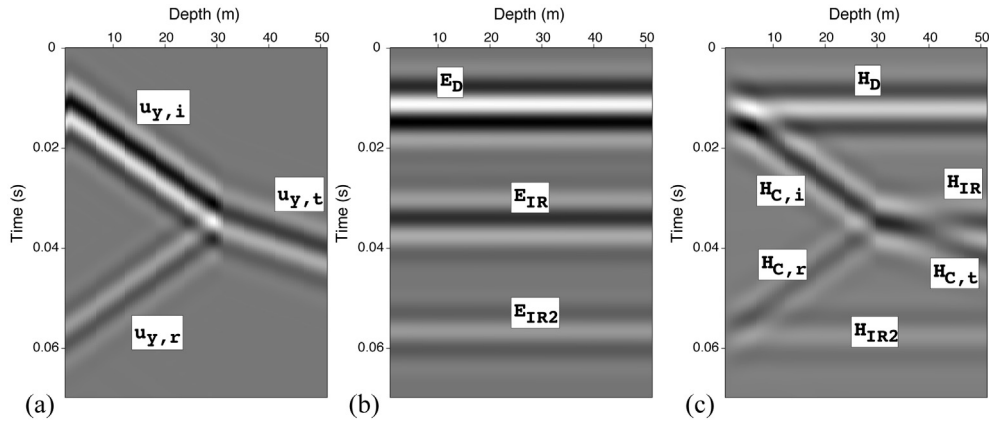


Fig. 2. Results obtained with the FE-algorithm using an infinite source along y , as described in Section 4.1. (a) Horizontal solid displacement $u_{y,j}$, $j = i, r, t$, i : incident, r : reflected, t : transmitted, (b) Horizontal electric field E_y , subscript D stands for direct, i.e. the field originated as a conversion at the source; subscript IR is associated to the interface response generated at 30.5 m depth, and the signal with subscript IR2 is assumed to be an interface response generated at the surface when $u_{y,r}$ reaches it at about 0.057 s, (c) horizontal magnetic field H_x ; the subscript D stands for direct, C for coseismic (i : incident, r : reflected and t : transmitted), subscript IR is associated to the magnetic interface response generated at 30.5 m depth, IR2 is the interface response generated at the surface, when $u_{y,r}$ reaches it.

Table 2
Permeability values associated with porosity values ranging from 2 to 24% computed using the empirical laws of Bourbié et al. (1987).

ϕ (%)	2	4	6	8	10	12
k_0 (m^2)	0	1.09×10^{-15}	2.79×10^{-14}	1.28×10^{-13}	2.50×10^{-13}	4.32×10^{-13}
ϕ (%)	14	16	18	20	22	24
k_0 (m^2)	6.86×10^{-13}	1.02×10^{-12}	1.46×10^{-12}	2.00×10^{-12}	2.66×10^{-12}	3.46×10^{-12}

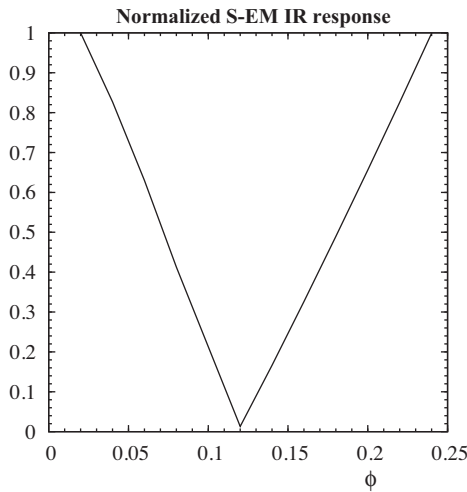


Fig. 3. Maximum S-EM IR amplitude versus porosity in the half-space of model described in Section 5.1.

The permeability values associated with the porosity values of the sandstone half-space are given in Table 2. For each set porosity and permeability values, we modeled the electric field along y , and measured the maximum S-EM IR value on the synthetic electrograms. Apart from porosity and permeability varying in the lower half-space, all other parameters are fixed.

In order to eliminate the influence of the source amplitude, the results obtained were normalized as follows: for each fixed parameter (here porosity) value, the portion of the signal corresponding to the interfacial response is isolated, and the maximum value of the maximum amplitude of all recorded IR's is selected. By varying the analysed parameter a set of these maxima is obtained. Finally, this set is normalised by dividing all values by the maximum value in it. The obtained results are displayed in Fig. 3. When the porosity value of the sandstone layer is 12%, meaning the same value as the upper sand layer, the interfacial response is zero because there is no

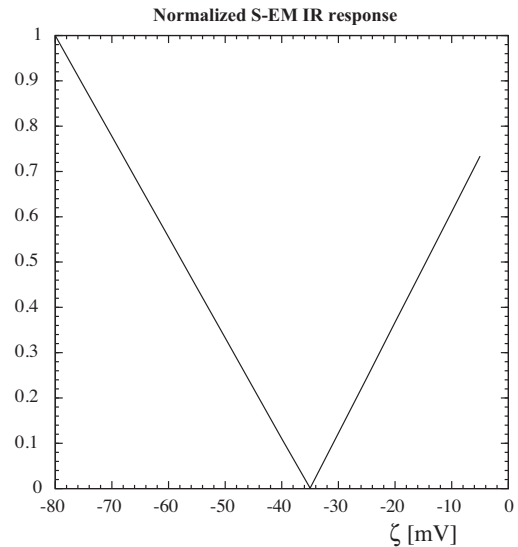


Fig. 4. Maximum S-EM IR amplitude versus ζ potential in the half-space of model described in Section 5.2.

contrast of any physical properties between the layers. When the porosity of the sand layer is either decreasing down to 2% or increasing up to 24% the maximum amplitude is increasing, because the contrast in porosity between the two layers is increasing.

5.2. ζ potential contrast

Following the same procedure as in the previous paragraph, we investigate the behaviour of the S-EM IR response when the ζ potential in the top layer remains fixed at -0.035 V, whilst its values are allowed to vary from -0.05 V to -0.07 V in the half-space.

Results are shown in Fig. 4: when both layers have the same zeta potential, there is no contrast in physical properties to induce an interfacial response. When the contrast in the zeta potential is

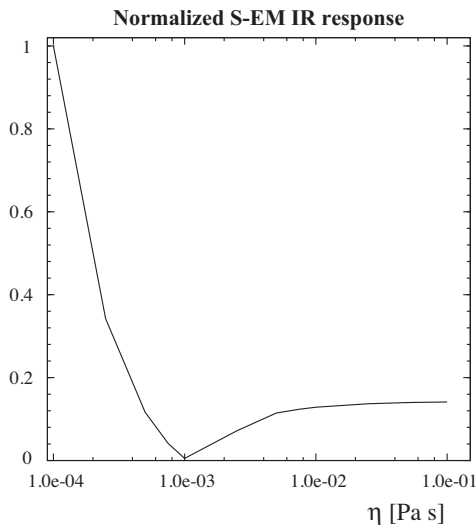


Fig. 5. Maximum S-EM IR amplitude versus viscosity η in the half-space of model described in Section 5.3.

increased, either by decreasing or increasing the zeta potential of the lower layer, then the interfacial response is increased.

5.3. Viscosity contrast

We finish this section by studying the dependence of the S-EM IR response when the viscosity $\eta = 10^{-3}$ Pa s in the upper-layer, whilst its values are allowed to vary from 10^{-4} Pa s to 10^{-1} Pa s in the half-space. Results are displayed in Fig. 5. As for the study of the other properties, when there is no contrast in physical properties there is no interfacial response. When the contrast in viscosity is increasing between the layers, the amplitude of the interface response increases. However, when the viscosity of the half space is larger than that of the upper layer, the amplitude of the response grows slowly, contrary to what happens when the viscosity of the half space is smaller than that of the top layer.

This sensitivity study shows that the amplitude of the interfacial response increases with an increasing contrast in porosity and zeta potential. This amplitude is also increased by an increasing contrast in viscosity when viscosity is decreased, which is the case when dealing with CO_2 at supercritical conditions.

6. Effect of a contrast between water-saturated sand and sandstone with various CO_2 saturations

In this section we model a contrast between an upper water-saturated layer and a lower semispace with various concentrations of CO_2 at supercritical conditions. We describe the results of the modelling coseismic magnetic field and the electric and magnetic interfacial responses induced by a shear-wave source.

6.1. Model including a layer with various CO_2 concentrations

In this section, we consider a simple model which consists of a 100 m thick layer on top of a half-space. Whilst the top layer remains fully saturated with water with a salinity coefficient $C_0 = 10^{-3}$ mol/l, the CO_2 saturation is allowed to vary in the half-space; the salinity is the same in both layers. The effective properties necessary for Pride's equations to remain valid when dealing with more than a single fluid phase are calculated following the formulae described in Section 4.1. As it is known from the CO_2 -sequestration literature, see -among others- (Kießling et al., 2010; Cairns et al., 2012), this gas is usually pumped in a supercritical state

into the subsurface. Therefore, we assume here that CO_2 is in the mentioned supercritical state and throughout the next sections we consider the following physical properties values for the carbon dioxide $\rho_{\text{CO}_2} = 505 \text{ kg/m}^3$, $\eta_{\text{CO}_2} = 1.5 \times 10^{-4} \text{ Pa s}$, $K_{\text{CO}_2} = 25 \text{ MPa}$, (Carcione et al., 2006) which as just mentioned correspond to it being in supercritical state meaning at pressure 10 MPa and temperature 37°C .

Although a hundred meters depth are not enough for this assumption to be valid (Kazemeini et al., 2010), we retain the mentioned depth value to keep a reasonable computational cost, because of the size of the model. Note that the following analysis would remain exactly the same if we increased the depth of the bottom of the top layer as much as necessary to reach the pressure and temperature conditions for the CO_2 to be in supercritical state.

It is known that when pumped into a reservoir a small portion of carbon dioxide dissolves in water (Carcione et al., 2006; Wang et al., 2013), forming weak carbonic acid which reacts with the present dissolved salt ions (Darwish and Hilal, 2010). This process alters the ζ potential (Moore et al., 2004), which in turn changes the electrokinetic coupling L_0 ; in the present work the zeta potential itself is not varying, but the effect of water-saturation is taken into account, as described above, by making L_0 saturation dependent. We assumed that the electrokinetic coupling is changed when the amount of CO_2 is increased and water expelled, as it changes when water-saturation is decreased, replaced by air (Eq. (13)).

We remark here that, as it can be inferred from Eq. (12), we consider the electrical conductivity of carbon dioxide σ_{CO_2} negligible compared to that of salty water. Although the CO_2 is not gaseous in our model, the supercritical CO_2 will increase the electrical resistivity of the layer, compared to water, as will do the air, with a lower increase induced by supercritical CO_2 than by gaseous CO_2 (Borner et al., 2013). Further studies should investigate, if possible, the electrokinetic coefficient in presence of supercritical CO_2 .

6.2. Results of the modelling: coseismic magnetic field

We first model the coseismic signal linked to the seismic propagation induced by the S-wave source (Fig. 6a). The maximum of each trace, as a function of depth, is pointed, and the maximum of these maxima is deduced, for each CO_2 saturation. Then this maximum is normalized by the value of the magnetic field for water-saturated conditions, each curve being normalized by its own maximum value. When no CO_2 -dependence on L_0 is assumed, meaning $S_w^n S(S_w) = 1$ in Eq. (13), the coseismic magnetic field linearly decreases with increasing CO_2 content. Even when L_0 remains constant, as the effective fluid density and conductivity diminish with increasing CO_2 saturation, so does the coseismic magnetic response, as can be seen from Fig. 6a, reflecting the behaviour predicted in Eq. (6).

When assuming a monotonous decrease of the electrokinetic coefficient with decreasing water-saturation as proposed by Perrier and Morat (2000), it is expected to observe a monotonous decrease of the coseismic magnetic field \mathbf{H} as foreseen in Eq. (6) and shown in Fig. 6a. Then, when another behaviour of the electrokinetic coefficient as a function of the water-saturation is assumed, as the one proposed by Allègre et al. (2010), we can observe first an increase in the coseismic magnetic field when the CO_2 saturation is increased and then a decrease with further increasing CO_2 saturation, as expected through the Eq. (6) where the magnetic field is proportional to the electrokinetic coefficient.

6.3. Results of the modelling: electric and magnetic interfacial responses

The interfacial response of the electric field and the magnetic field are shown in Figs. 6b and c. The electric interfacial response

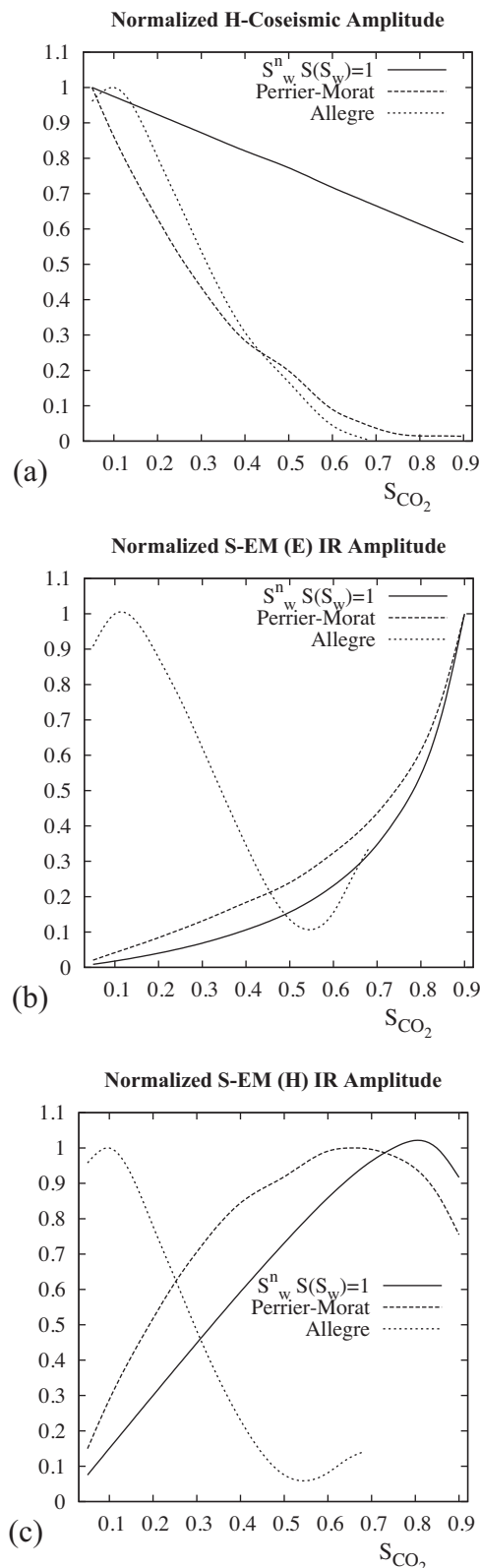


Fig. 6. CO₂ saturation dependence of the (a) Coseismic magnetic response, (b) S-EM interface response for the electric field and (c) S-EM interface response for the magnetic field for the different electrokinetic coupling models assumed in this work.

is increasing with increasing CO₂ saturation, for both cases of $S_w^n S(S_w) = 1$ and for the model from Perrier and Morat (2000). Using the model of Allègre et al. (2010) the electric interfacial response first increases to reach a maximum for a CO₂ saturation of about 12% and then decreases for a CO₂ saturation in the range 12–55% before increasing for a CO₂ saturation in the range 55–70%. The magnetic interfacial response increases when the CO₂ saturation increases up to about 70% for both cases of $S_w^n S(S_w) = 1$ and for the model from Perrier and Morat (2000), before decreasing with further increase of CO₂ saturation. Using the model of Allègre et al. (2010) the magnetic interfacial response first increases to reach a maximum for a CO₂ saturation of about 10% and then decreases for a CO₂ saturation in the range 10–55% before increasing for a CO₂ saturation in the range 55–70%. Therefore the relative maximum interfacial response, for both the electric field and the magnetic field, is different according to the different models of the CO₂-dependence of the electrokinetic coupling, and occurs either around 10% or 70–90% of CO₂ saturation.

We can compare the behaviour of the interfacial response of the electrical field observed here with the one observed for the study of a contrast in water-saturation using a P-wave source rather than a S-wave source (Warden et al., 2013). The electric interfacial response showed also an increase and then a decrease with increasing air-content using the model of Allègre et al. (2010), but showed a maximum at about 30% (Fig. 9a in Warden et al. (2013)) rather than 12% (see Fig. 6b). The electrical interfacial response using the model of Perrier and Morat (2000) also showed a continuous increase with increasing air-content, although the curvatures are different.

These results do not show the relative amplitudes according to the different models. Consequently we normalized the magnetic coseismic field, the electric interfacial response and the magnetic interfacial response obtained for both models by the field values obtained using the electrokinetic coupling L_0 assuming $S_w^n S(S_w) = 1$ in Eq. (13). These results show that the amplitude of the coseismic magnetic field using the model from Allègre et al. (2010) can be a factor 10 larger than the results using the model from Perrier and Morat (2000) for CO₂ saturation around 10% (Fig. 7). The electric interfacial response using the model from Allègre et al. (2010) can be about 50 times larger than the results using the model from Perrier and Morat (2000) for CO₂ saturation around 5% (Fig. 8). The magnetic interfacial response using the model from Allègre et al. (2010) can be also about 50 times larger than the results using the model from Perrier and Morat (2000) for CO₂ saturation around 5% (Fig. 9). Comparing Figs. 7 and 9 we can deduce that the ratio between the IR amplitude and coseismic amplitude of the magnetic field is about 45 and 6 using the model from Allègre et al. (2010) and Perrier and Morat (2000) respectively.

We can notice that in both considered cases for the CO₂-dependence of the electrokinetic coupling model, the magnetic IR is larger than the coseismic magnetic field, which is not usually the case for the electric field using a P-wave source. Therefore measuring the magnetic interfacial response induced by a S-wave source, could be an efficient method to detect the interface between a water-saturated layer and a partially CO₂ saturated layer.

Moreover, as the electric coseismic signal induced by an S-wave source is absent, the electric IR is easier to be detected. Therefore an efficient method to detect different CO₂ saturations would be to measure the electric interfacial response using a S-wave source. The amplitude of the response would be up to 300 times higher than the amplitude of the signal induced by a water-saturated medium, depending on the model used for the CO₂-dependence of the electrokinetic, in the saturation range 5–15%, and 10–100 times higher in the 15–40% CO₂ saturation range.

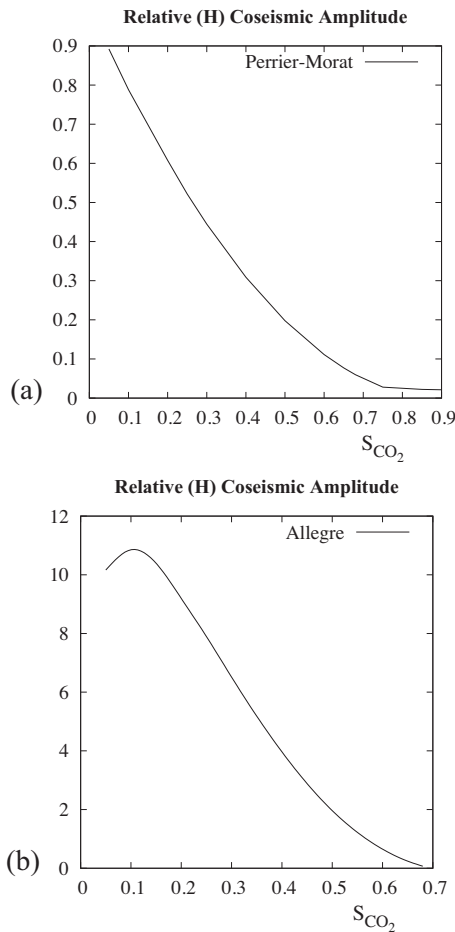


Fig. 7. Relative amplitude of the coseismic magnetic field for (a) Perrier–Morat model and (b) Allègre model; both cases are compared to the amplitude of the H-coseismic response when using the electrokinetic coupling L_0 assuming $S_w^0 S(w) = 1$ in Eq. (13).

7. Seismo-electromagnetic conversions induced in a CO₂ reservoir with a seal layer

Let us consider now a new model, shown in Fig. 10, in which we intersperse a 10 m deep seal layer of very low permeability among a 100 m deep layer whose top boundary is the air–soil interface, and a semispace in which CO₂ saturation can be changed. Indeed clay layers can be present as thin intra-reservoir shales. They act as main barriers to the upward migration of CO₂ beneath which the CO₂ accumulates at high saturations (Arts et al., 2004).

The three layers parameters are displayed in Table 3; we remark that the permeability of the seal layer is four orders of magnitude smaller than the one of the top layer and the semi-space. In order to better approximate a possible carbon dioxide deposition site, we strongly increase the NaCl concentration in the water saturating the semi-space, therefore enhancing its electrical conductivity, which yields a bulk conductivity of $\sigma = 0.12$ [S/m] at full water saturation. The semi-space is then the most electrically conductive, the seal layer has a smaller bulk conductivity including a surface conductivity, and the top layer has the lowest bulk conductivity. The zeta potential, which depends on the fluid conductivity is very small within the briny semi-space. It is about -3 mV within the seal and -70 mV within the top layer. This configuration leads to an electrokinetic coupling in the seal layer about 16 times smaller than the value of the one corresponding to the top layer, and of about twice that of the semi-space. The electrokinetic coupling does not reflect here only the zeta potential (itself linked

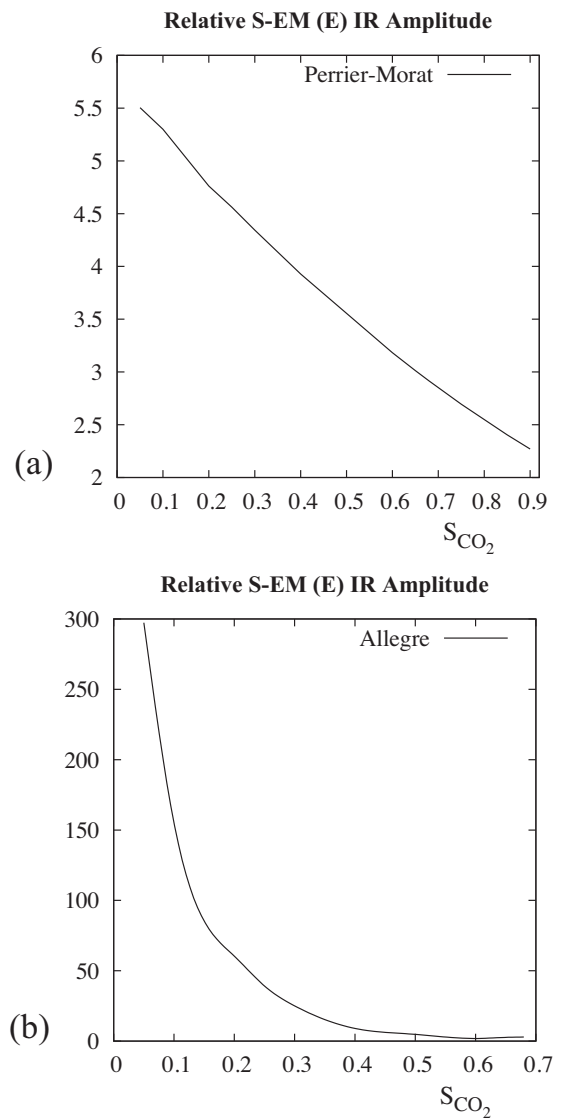


Fig. 8. Relative amplitude of the interface response electric field for (a) Perrier–Morat model and (b) Allègre model; both cases are compared to the amplitude of the S-EM (E) response when using the electrokinetic coupling L_0 assuming $S_w^0 S(w) = 1$ in Eq. (13).

to the fluid conductivity), but also the permeability (see Eq. (3)) which is very low in the half-space. Therefore the contrast in the electrokinetic coupling is higher between the semi-space and the seal layer than the one between the top layer and the seal layer.

According to the analysis performed in previous sections, an interface response is expected to arise at both seal interfaces, with potentially a larger signal between the semi-space and the seal layer because of a larger contrast in the electrokinetic couplings. However, the method is not expected to resolve them, because the two IR’s are separated about 7 milliseconds ($v_s = 1700$ m/s), the width of the central peak of the source being about 4.5 ms. Recall, however, that we are not mainly interested in determining the width of the seal, but in what lies beneath it. Notice that previous numerical studies (Pride and Garambois, 2005) have shown that for thin enough layers, the Interface Response can attain very large values.

In Fig. 11 we display a borehole gather for (a) the seismic waves, (b) the electric field and (c) the magnetic field, considering a 65% carbon dioxide saturation in the semispace. It can be seen in the leftmost picture that contrary to the seismic response of our first

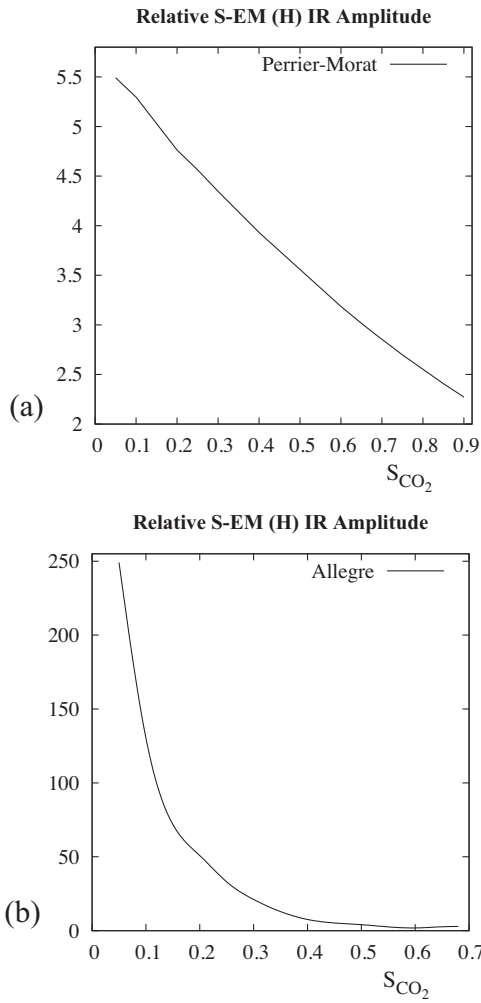


Table 3

Properties of the model analysed in Section 7, the \ast value for the electrical conductivity for the semispace corresponds to the water saturated case; the value for an effective fluid mixture with $S_{CO_2} = 65\%$ is equal to 1.59×10^{-2} .

	Top layer	Seal	Semispace
ϕ (%)	20	20	20
m	1.7	1.7	1.7
k_0 (m ²)	0.5×10^{-13}	0.4×10^{-17}	0.5×10^{-13}
k_s (Pa)	36×10^9	36×10^9	36×10^9
k_{fr} (Pa)	5.40×10^9	5.40×10^9	5.40×10^9
G_{fr} (Pa)	5.80×10^9	5.80×10^9	5.80×10^9
ρ_s (kg/m ³)	2.6×10^3	2.6×10^3	2.6×10^3
κ_s	4	4	4
k_w (Pa)	2.27×10^9	2.27×10^9	2.27×10^9
η_w (Pa s)	1×10^{-3}	1×10^{-3}	1×10^{-3}
ρ_w (kg/m ³)	1×10^3	1×10^3	1×10^3
κ_w	80	80	80
C_0 (mol/L)	1×10^{-3}	4×10^{-2}	0.4
k_{CO_2} (Pa)	–	–	25×10^6
η_{CO_2} (Pa s)	–	–	1.5×10^{-5}
ρ_{CO_2} (kg/m ³)	–	–	505
κ_{CO_2}	–	–	1
σ (S/m)	3.41×10^{-4}	1.55×10^{-3}	$\ast 0.12$
ζ (V)	–0.07	–0.027	–0.0023
T (K)	298	298	298

and magnetic interface response H_{IR} are clearly observable, raised simultaneously with the arrival of the incident seismic wave to the interface between the top and seal layers, at about 0.06 s. The electric IR can be detected within the whole depth range, whereas the

Fig. 9. Relative amplitude of the Interface Response magnetic field for (a) Perrier–Morat model and (b) Allègre model; both cases are compared to the amplitude of the S-EM (H) response when using the electrokinetic coupling L_0 assuming $S_w^0 S(w) = 1$ in Eq. (13).

example, shown in Fig. 2(a), the amplitude of the reflected seismic wave is much smaller than the incident wave, due to the similar mechanical properties of the seal layer and the semi-space, recall that they have just different permeabilities and different fluids saturating them. However, both electric interface response E_{IR}

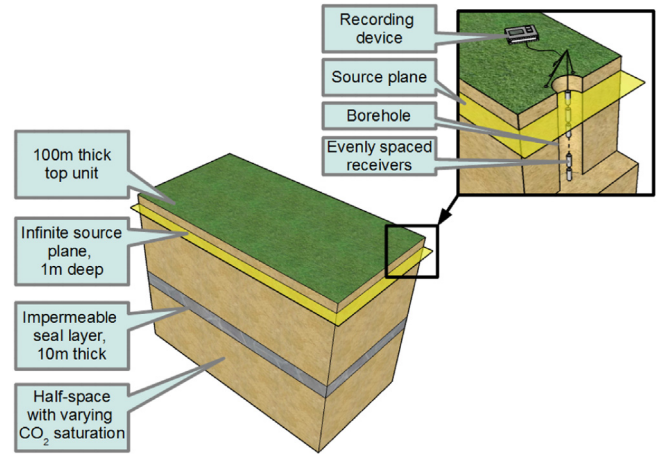


Fig. 10. Model with a seal layer.

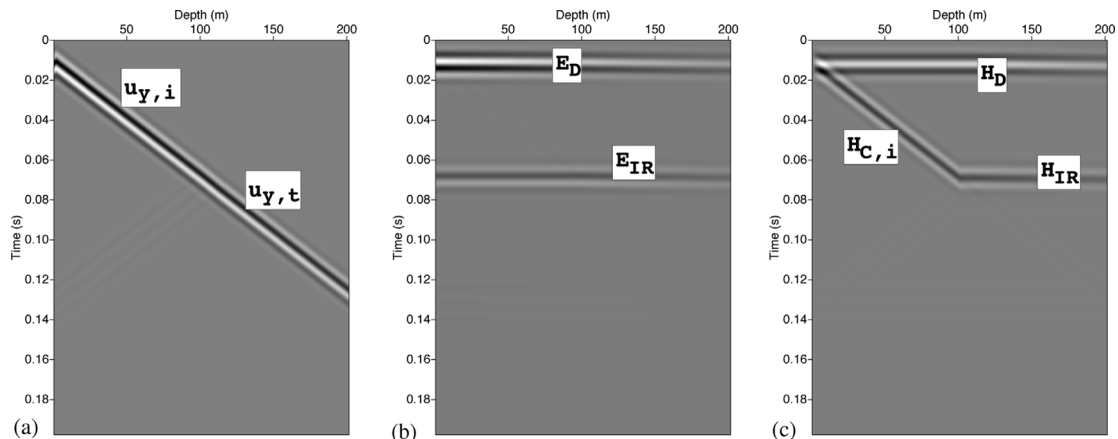


Fig. 11. Results for the model of CO₂ reservoir with a seal layer. CO₂ saturation is 65% within the semi-space (below depth 100 m). Horizontal displacement u_y (a), horizontal electric field E_y (b) and horizontal magnetic Field H_x (c) obtained with the FE-algorithm using an infinite source along y , as described in Section 4.1.

magnetic IR can be detected only at depths below the seal layer. Also discernible is the coseismic magnetic field (see Fig. 11c), traveling within the incident, reflected and transmitted seismic shear waves.

With the goal of detecting possible changes in the CO₂ saturation within the semi-space, the magnetic and electric interfacial responses were calculated for CO₂ saturations of 5%, 25% and 65%. In Fig. 12 we show time windows highlighting the difference between the magnetic field interface responses of two different CO₂ saturations; in (a) we take the difference between 65% and 5% saturations and in (b) we take the difference between 65% and 25% saturations. The relative differences normalised by the value of the IR at 65% of CO₂ saturation (the maximum of the maxima of all traces is taken into account, as previously explained) show a variation of 30% when saturation varies from 65% to 5%, and a variation of 22% when saturation varies from 65% to 25%. These results show us that even when the interface response of the bottom boundary of the seal is “entangled” with the one produced at its top boundary, the recorded magnetic IR in the well receivers – located below the

lowest interface – are very sensitive to carbon dioxide saturation changes.

In Fig. 13 we show the time windows highlighting the differences between the electric field interface responses of the same two different CO₂ saturations. The relative differences normalised by the value of the IR at 65% of CO₂ saturation show a variation of 62% when saturation varies from 65% to 5%, and a variation of 52% when saturation varies from 65% to 25%. Therefore the sensitivity of the electric IR to the CO₂ saturation variations is larger than the sensitivity of the magnetic IR.

The detection of the variation of CO₂ concentration could be therefore performed by measuring the electric and magnetic field in boreholes. The magnetic field measured below the interface could detect the magnetic IR induced by the contrast of the seal layer and the semi-space; the electric field could be measured below and above the interface. Moreover, as the coseismic part of the electric field is absent when using a S-wave source, the electric IR may be easier to be detected than the magnetic IR. However if the electric ambient noise is high, the electric IR may be still difficult to

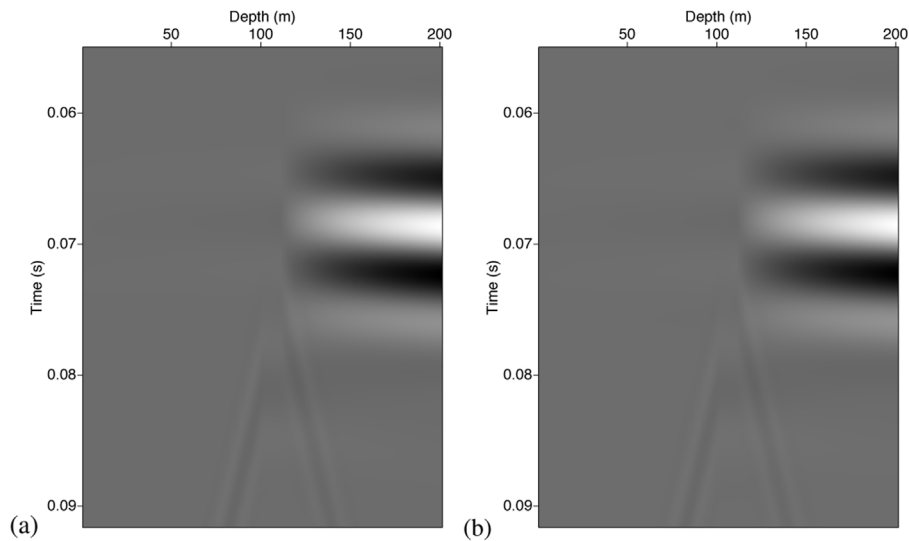


Fig. 12. From the magnetic field well gather, – Fig. 11(c) – we select a time window, displaying the difference of the magnetic field IR response between two different CO₂ saturations, namely 5% and 65% (a); while in (b) the same result as in (a) is displayed, but the difference is taken considering CO₂ saturations of 25% and 65%.

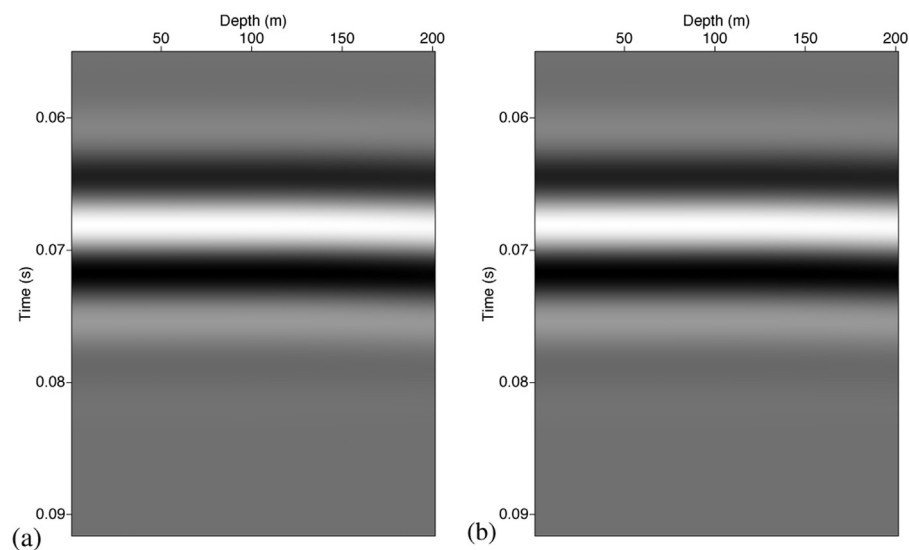


Fig. 13. From the electric field well gather, – Fig. 11(b) – we select a time window, displaying the difference of the electric field IR response between two different CO₂ saturations, namely 5% and 65% (a); while in (b) the same result as in (a) is displayed, but the difference is taken considering CO₂ saturations of 25% and 65%.

measure, even if a large variation is expected as a function of the CO₂ concentration. The measurement of the magnetic field below the interface may still help to detect the CO₂ saturation variations, because the magnetic IR is larger than the coseismic magnetic signal, and because of the sensitivity of the magnetic IR which is still noticeable although lower than the one of the electric IR.

8. Conclusions

In this paper we numerically analyzed shear wave driven seismoelectromagnetic conversions in a surface-to-borehole layout, using a one dimensional finite elements code. Sensitivity analysis of the S-EM IR for porosity, permeability, zeta potential and viscosity were performed for a simple tabular medium, and normalized responses were used in these analysis, in order to make them independent of the physical source used by the employed method.

It was observed that –as expected– no contrast in the properties leads to the absence of interface response; and that the response increases when the contrast in porosity and zeta potential is increased, while for relatively large values of the viscosity the response is asymptotically constant.

We studied also the behaviour of the electromagnetic responses for a model considering realistic partial CO₂ saturations. We used the extended Pride's formulation for the electrokinetic coupling for the case of partially saturated media recently presented in [Warden et al. \(2013\)](#) to take into account the presence of carbon dioxide in our model. Moreover, we studied the magnetic coseismic response and electric and magnetic interface responses using Perrier-Morat and Allègre formulas in the partial CO₂ saturation version of the electrokinetic coupling. We observed that the relative maximum in the interface response for both the electric and magnetic fields is different according to the different models of the CO₂-dependence for the electrokinetic coupling, and occurs at either around 10% or 70–90% of carbon dioxide saturation.

These results are obtained assuming that the injection of supercritical CO₂ in water-saturated sandstone decreases the electrical conductivity, as shown by [Borner et al. \(2013\)](#) during short time experiments. However it has to be noted that the injection of supercritical CO₂ in brine solutions increases its electrical conductivity, because of the dissolution of CO₂ in water, with a larger effect on fresh water solution than on saline solutions ([Borner et al., 2013](#)). This effect was assumed not to take place in the short-time experiments. Therefore considering long-time period of CO₂ storage and dissolution process, further studies may consider different hypotheses on the effect of supercritical CO₂ on the electrical conductivity.

When studying the magnetic and electric interface responses of a model for a sealed CO₂ reservoir with different saturations, we observed that they are sensitive to CO₂ saturation variations, even when they are superimposed with the interface response of the boundary between the overburden and the seal; the sensitivity of the electric IR is higher than the one of the magnetic IR. The electric IR variations are observable with recorders located in the reservoir above or below the seal layer, whereas the magnetic IR is only observed below the seal layer. Both magnetic and electric field measured in borehole could detect the variations of CO₂ saturation below the seal.

Noting that up to now seismomagnetic signals were recorded in experiments performed in the laboratory by [Bordes et al. \(2008\)](#) or under special conditions ([Gaffet et al., 2003](#)), and further developments are needed to measure seismomagnetic signals in the field, we consider that an efficient method to detect a CO₂ saturation in the range 5–40% would be to measure the electric interfacial response using a S-wave source, expecting a

signal 5–300 higher than the signal induced by a water-saturated medium.

We expect the novel results presented in this work will be followed by other necessary developments, such as the analysis of the absolute amplitudes of the IR responses, to show if they are large enough to be detected. Moreover more realistic geological environments should be modeled, eventually leading to a new monitoring tool which complements the existing ones.

Acknowledgements

This work was partially supported by a CNRS (INSU) – CONICET International Collaboration Grant, and by Université de Strasbourg.

Appendix A. One dimensional SHTE equations

Consider Pride's equations in the equivalent form given in [Zyserman et al. \(2012\)](#)

$$(\sigma + i\epsilon\omega)E - \nabla \times H + L(\omega)\eta_f k^{-1}(\omega)[i\omega u^f - L(\omega)E] = -J_e^{ext}, \quad (\text{A.1})$$

$$\nabla \times E + i\omega\mu H = -J_m^{ext}, \quad (\text{A.2})$$

$$-\omega^2 \rho_b u^s - \omega^2 \rho_f u^f - \nabla \cdot \tau(u) = F^{(s)}, \quad (\text{A.3})$$

$$-\omega^2 \rho_f u^s + \eta_f k^{-1}(\omega)[i\omega u^f - L(\omega)E] + \nabla p_f = F^{(f)}, \quad (\text{A.4})$$

$$\tau_{lm}(u) = 2G_{fr} \varepsilon_{lm}(u^s) + \delta_{lm}(\lambda_c \nabla \cdot u^s + \alpha K_{av} \nabla \cdot u^f), \quad (\text{A.5})$$

$$p_f(u) = -\alpha K_{av} \nabla \cdot u^s - K_{av} \nabla \cdot u^f. \quad (\text{A.6})$$

Here τ and ε are the stress and strain tensors, $\rho_b = \phi\rho_f + (1 - \phi)\rho_s$ the bulk density, K_{av} is the fluid-storage coefficient and αK_{av} is the Biot coupling coefficient, with $\alpha = 1 - K_{fr}/K_s$. In the seismic frequency regime, for most fluid saturated rocks, displacement currents can be safely neglected against conduction currents in the factor multiplying the electric field E in the first term of Eq. (A.1). Besides, as it has been demonstrated ([Haines and Pride, 2006](#)), if $\eta L^2(\omega)/(\sigma k(\omega)) \ll 1$, the electroosmotic feedback can be neglected in Biot's equations, and the latter decouples from Maxwell's equations. As we are dealing with just seismic shear sources, we set the electromagnetic sources, and the seismic source acting upon the fluid to zero, $J_m^{ext} = J_e^{ext} = F^{(f)} = 0$. Moreover, as $F^{(s)}$ is considered to be a shearing force parallel to the y axis acting on a horizontal infinite plane upon a horizontally layered Earth, only solid displacements $u^s = u_y^s(z, \omega)$ and fluid displacements $u^f = u_y^f(z, \omega)$ are possible. Therefore, we have $E = E_y(z, \omega)$ and $H = H_x(z, \omega)$. Under these considerations, Eqs. (A.1)–(A.6) can be rewritten as

$$\sigma E - \partial_z H = i\omega\eta_f k^{-1}(\omega)L(\omega)u^f, \quad (\text{A.7})$$

$$\partial_z E + i\omega\mu H = 0 \quad (\text{A.8})$$

$$-\omega^2 \rho_b u^s - \omega^2 \rho_f u^f - \partial_z(G_{fr} u^s) = F^s, \quad (\text{A.9})$$

$$-\omega^2 \rho_f u^s + i\omega\eta_f k^{-1}(\omega)u^f = 0, \quad (\text{A.10})$$

where we used ∂_z to denote the derivative with respect to z . Notice that, although we have not considered it, in the seismic frequency range it is usual to take the low frequency limit for the electrokinetic coupling coefficient and the dynamic permeability; in this case we would have $i\omega(\eta_f/k_0)L_0 u^f$ as the r.h.s. of Eq. (A.7) and $i\omega\eta_f k^{-1}(\omega) \approx (-\omega^2 g_0 + i\omega\eta/k_0)$ in Eq. (A.10); in this last expression g_0 is the mass coupling coefficient. Finally, following [Santos et al. \(2004\)](#), we express $F^{(s)}$ as

$$F^{(s)}(z, \omega) = F(\omega)\partial_z \delta(z - z_f). \quad (\text{A.11})$$

Here $F(\omega)$ is the Fourier transform of the source time signature, and the Dirac's delta derivative must be understood in the distributional sense; by z_f we denote the depth at which the source is located.

The set of Eqs. (A.7)–(A.10) must be completed with appropriate boundary conditions. For Maxwell's equations we use absorbing boundary conditions (ABC's) at the top and bottom boundaries, for Biot's equations we use the free boundary condition for the air–soil interface and again ABC's at the bottom boundary; see Zyserman et al. (2010, 2012) and references therein for details. In the present case they read, for Maxwell's equations and Biot's equations respectively:

$$(1 - i)\sqrt{\frac{\sigma}{2\omega\mu}}E - \nu H = 0, \quad (\text{A.12})$$

where ν takes the value -1 at the top boundary and the value 1 at the bottom one,

$$\partial_z u^s = 0 \quad \text{Top boundary,} \quad (\text{A.13})$$

$$-G_{fr}\partial_z u^s = i\omega(\rho_b - \rho_f^2/g(\omega))\sqrt{\frac{G_{fr}}{\rho_b - \rho_f^2/g(\omega)}}, \quad (\text{A.14})$$

Bottom boundary,

where $g(\omega) = (1/\omega)\text{Im}(\eta/k(\omega))$. As already stated, the system of Eqs. (A.7)–(A.14) is solved by means of a finite elements procedure.

References

- Aizawa, K., Uyeshima, M., Nogami, K., 2008. Zeta potential estimation of volcanic rocks on 11 island arc-type volcanoes in Japan: implication for the generation of local self-potential anomalies. *J. Geophys. Res.* 113, B02201.
- Allègre, V., Jouniaux, L., Lehmann, F., Sailhac, P., 2010. Streaming potential dependence on water-content in Fontainebleau sand. *Geophys. J. Int.* 182, 1248–1266.
- Allègre, V., Lehmann, F., Ackerer, P., Jouniaux, L., Sailhac, P., 2012. Modelling the streaming potential dependence on water content during drainage: 1. A 1D modelling of SP using finite element method. *Geophys. J. Int.* 189, 285–295.
- Arts, R., Eiken, O., Chadwick, A., Zweigel, P., van der Meer, L., Zinszner, B., 2004. Monitoring of CO₂ injected at Sleipner using time lapse seismic data. *Energy* 19, 1383–1392.
- Bale, R., Marchand, T., Wilkinson, K., Wikel, K., Kendall, R., 2013. The signature of shear-wave splitting: theory and observations on heavy oil data. *Lead. Edge* 32 (1), 6434–6443.
- Biot, M.A., 1956a. Theory of propagation of elastic waves in a fluid-saturated porous solid: I. Low frequency range. *J. Acoust. Soc. Am.* 28 (2), 168–178.
- Biot, M.A., 1956b. Theory of propagation of elastic waves in a fluid-saturated porous solid: II. High frequency range. *J. Acoust. Soc. Am.* 28 (2), 178–191.
- Biot, M.A., 1962. Mechanics of deformation and acoustic propagation in porous media. *J. Appl. Phys.* 34 (1), 36–40.
- Block, G.I., Harris, J.G., 2006. Conductivity dependence of seismoelectric wave phenomena in fluid-saturated sediments. *J. Geophys. Res.* 111, B01304.
- Bordes, C., Jouniaux, L., Garambois, S., Dietrich, M., Pozzi, J.-P., Gaffet, S., 2008. Evidence of the theoretically predicted seismo-magnetic conversion. *Geophys. J. Int.* 174, 489–504.
- Borner, J., Herdegen, V., Repke, J., Spitzer, K., 2013. The impact of CO₂ on the electrical properties of water bearing porous media-laboratory experiments with respect to carbon capture and storage. *Geophys. Prospect.* 61, 446–460.
- Bourbié, T., Coussy, O., Zinszner, B., 1987. *Acoustic of porous media*. Institut Francais du pétrole publications, Ed Technip.
- Brie, A., Pampuri, F., Marsala, A., Meazza, O., 1995. *Shear Sonic Interpretation in Gas Bearing Sands*. Society of Petroleum Engineers.
- Brovelli, A., Cassiani, G., Dalla, E., Bergamini, F., Pitea, D., Binley, A.M., 2005. Electrical properties of partially saturated sandstones: novel computational approach with hydrogeophysical applications. *Water Resour. Res.* 41, 12pp.
- Butler, K., Dupuis, J., Kecip, A., 2007. Signal to noise improvements in seismoelectrics data acquisition. *Ground Borehole Geophys. Methods* 111, 3753–3755.
- Butler, K., Russell, R., Kecip, A., Maxwell, M., 1996. Measurements of the seismoelectric response from a shallow boundary. *Geophysics* 61, 1769–1778.
- Butler, K.E., Russell, R.D., 2003. Cancellation of multiple harmonic noise series in geophysical records. *Geophysics* 68, 1083–1090.
- Cairns, G., Jakubowicz, H., Lonergan, L., Muggerridge, A., 2012. Using time-lapse seismic monitoring to identify trapping mechanisms during CO₂ sequestration. *Int. J. Greenhouse Gas Control* 11, 316–325.
- Carcione, J., Picotti, S., Gei, D., Michelini, R., 2012. Cross-hole electromagnetic and seismic modeling for CO₂ detection and monitoring in a saline aquifer. *J. Petrol. Sci. Eng.* 100, 162–172.
- Carcione, J., Picotti, S., Gei, D., Rossi, G., 2006. Physics and seismic modeling for monitoring CO₂ storage. *Pure Appl. Geophys.* 163 (1), 175–207.
- Chadwick, R., Noy, D., Arts, R., Eiken, O., 2009. Latest time-lapse seismic data from sleipner yield new insights into CO₂ plume development. *Energy Proc.* 1 (1), 2103–2110.
- Chadwick, R., Williams, G., Dellepine, N., Clochard, V., Labad, K., Sturton, S., Bud-densiek, M., Dillen, M., Nikken, M., Lima, A.L., Arts, R., Neele, F., Rossi, G., 2010. Quantitative analysis of time-lapse seismic monitoring data at the Sleipner CO₂ storage operation. *Lead. Edge* 29 (2), 170–177.
- Chen, B., Mu, Y., 2005. Experimental studies of seismoelectric effects in fluid-saturated porous media. *J. Geophys. Eng.* 2, 222–230.
- Darwish, N., Hilal, N., 2010. A simple model for the prediction of CO₂ solubility in H₂-NaCl system at geological sequestration conditions. *Desalination* 260, 114–118.
- Davis, T., Bibolova, A., O'Brien, S., Klepacki, D., Robinson, H., 2013. Prediction of residual oil saturation and cap-rock integrity from time-lapse, multicomponent seismic data, Delhi Field, Louisiana. *Lead. Edge* 32 (1), 6434–6443.
- Dupuis, J.C., Butler, K.E., Kecip, A.W., 2007. Seismoelectric imaging of the vadose zone of a sand aquifer. *Geophysics* 72, A81–A85.
- Ellis, M., 2010. The potential of controlled source electromagnetic surveying in CO₂ storage monitoring. *SEG Expand. Abstr.* 29, 843–847.
- Fabriol, H., Bitri, A., Bourgeois, B., Delatre, M., Girard, J., Pajot, G., Rohmer, J., 2011. Geophysical methods for CO₂ plume imaging: comparison of performances. *Energy Proc.* 4, 3604–3611.
- Fischer, S., Liebscher, A., Lucia, M.D., Hecht, L., 2013. Reactivity of sandstone and siltstone samples from the Ketzin pilot CO₂ storage site-Laboratory experiments and reactive geochemical modeling. *Environ. Earth Sci.* 70, 3687–3708.
- Gaffet, S., Guglielmi, Y., Virieux, J., Waysand, G., Chwala, A., Stolz, R., Emblanch, C., Auguste, M., Boyer, D., Cavaillou, A., 2003. Simultaneous seismic and magnetic measurements in the low-noise underground laboratory (LSBB) of rustrel, france, during the 2001 January 26 Indian earthquake. *Geophys. J. Int.* 155, 981–990.
- Gao, Y., Hu, H., 2010. Seismoelectromagnetic waves radiated by a double couple source in a saturated porous medium. *Geophys. J. Int.* 181, 873–896.
- Garambois, S., Dietrich, M., 2001. Seismoelectric wave conversions in porous media: field measurements and transfer function analysis. *Geophysics* 66, 1417–1430.
- Garambois, S., Dietrich, M., 2002. Full waveform numerical simulations of seismo-electromagnetic wave conversions in fluid-saturated stratified porous media. *J. Geophys. Res.* 107 (B7), ESE 5-1.
- Girard, J., Coppo, N., Rohmer, J., Bourgeois, B., Naudet, V., Schmidt-Hattenberger, C., 2011. Time-lapse CSEM monitoring of the ketzin (Germany) CO₂ injection using 2 x MAM configuration. *Energia Proc.* 4, 3322–3329.
- Glover, P., Walker, E., Ruel, J., Tardif, E., 2012. Frequency-dependent streaming potential of porous media-Part 2: Experimental measurement of unconsolidated materials. *Int. J. Geophys.*, 17, Article ID 728495.
- Gomez, J., Ravazzoli, C., 2011. AVA Seismic reflectivity analysis in carbon dioxide accumulations: sensitivity to CO₂ phase and saturation. *J. Appl. Geophys.* 72, 93–100.
- Guan, W., Hu, H., 2008. Finite-difference modeling of the electroseismic logging in a fluid-saturated porous formation. *J. Comput. Phys.* 227, 5633–5648.
- Guan, W., Hu, H., Wang, Z., 2013. Permeability inversion from low-frequency seismoelectric logs in fluid-saturated porous formations. *Geophys. Prospect.* 61, 120–133.
- Guichet, X., Jouniaux, L., Catel, N., 2006. Modification of streaming potential by precipitation of calcite in a sand-water system: laboratory measurements in the pH range from 4 to 12. *Geophys. J. Int.* 166, 445–460.
- Guichet, X., Jouniaux, L., Pozzi, J.-P., 2003. Streaming potential of a sand column in partial saturation conditions. *J. Geophys. Res.* 108 (B3), 2141.
- Haartsen, M.W., Pride, S., 1997. Electroseismic waves from point sources in layered media. *J. Geophys. Res.* 102, 769, 24,745–24.
- Haines, S., 2004. *Seismoelectric imaging of shallow targets*, Ph.D. thesis. Stanford University.
- Haines, S.H., Pride, S.R., 2006. Seismoelectric numerical modeling on a grid. *Geophysics* 71 (6), 57–65.
- Haines, S.S., Pride, S.R., Klemperer, S.L., Biondi, B., 2007. Seismoelectric imaging of shallow targets. *Geophysics* 72, G9–G20.
- Ishido, T., Mizutani, H., 1981. Experimental and theoretical basis of electrokinetic phenomena in rock water systems and its applications to geophysics. *J. Geophys. Res.* 86, 1763–1775.
- Ishido, T., Pritchett, J., Toshi, T., Nishi, Y., Nakanishi, S., 2013. Monitoring underground migration of sequestered CO₂ using self-potential methods. *Energy Proc.* 37, 4077–4084.
- Jackson, M.D., 2010. Multiphase electrokinetic coupling: insights into the impact of fluid and charge distribution at the pore scale from a bundle of capillary tubes model. *J. Geophys. Res.* 115, B07206.
- Johnson, D.L., Koplik, J., Dashen, R., 1987. Theory of dynamic permeability in fluid saturated porous media. *J. Fluid. Mech.* 176, 379–402.
- Jouniaux, L., Bordes, C., 2012. Frequency-dependent streaming potentials: a review. *Int. J. Geophys.*, 11, Article ID 648781.
- Jouniaux, L., Ishido, T., 2012. Electrokinetics in Earth Sciences: a tutorial. *Int. J. Geophys.*, 16, Article ID 286107.
- Jouniaux, L., Lallemand, S., Pozzi, J., 1994. Changes in the permeability, streaming potential and resistivity of a claystone from the Nankai prism under stress. *Geophys. Res. Lett.* 21, 149–152.
- Jouniaux, L., Pozzi, J.-P., Berthier, J., Massé, P., 1999. Detection of fluid flow variations at the Nankai trough by electric and magnetic measurements in boreholes or at the seafloor. *J. Geophys. Res.* 104, 29293–29309.
- Kazemeini, S., Juhlin, C., Fomel, S., 2010. Monitoring CO₂ response on surface seismic data; a rock physics and seismic modeling feasibility study at the CO₂ sequestration site, Ketzin, Germany. *J. Appl. Geophys.* 71, 109–124.

- Kiessling, D., Schmidt-Hatterberger, C., Schuett, H., Schilling, F., Krueger, K., Schoebel, B., Dankwardt, E., Kummerow, J., 2010. Geoelectrical methods for monitoring geological CO₂ storage: first results from cross-hole and surface-downhole measurements from the CO₂SINK test site at Ketzin (Germany). *Int. J. Greenhouse Gas Control* 4, 816–826.
- Kim, J., Nam, M., Matsuoka, T., 2013. Estimation of CO₂ saturation during both CO₂ drainage and imbibition processes based on both seismic velocity and electrical resistivity measurements. *Geophys. J. Int.*
- Liu, Z., Zhang, L.Y.X., Liu, Z., Wu, H., 2008. A laboratory seismoelectric measurement for the permafrost model with a frozen-unfrozen interface. *Geophys. Res. Lett.* L21 (35), 404.
- Maineult, A., Jouniaux, L., Bernabé, Y., 2006. Influence of the mineralogical composition on the self-potential response to advection of KCl concentration fronts through sand. *Geophys. Res. Lett.* 33, L24311.
- Martens, S., Kempka, T., Liebscher, A., Lüth, S., Möller, F., Myrntinen, A., Norden, B., Schmidt-Hattenberger, C., Zimmer, M., Kühn, M., 2012. Europe's longest-operating on-shore CO₂ storage site at Ketzin, Germany: a progress report after three years of injection. *Environ. Earth Sci.* 67, 323–334.
- Martens, S., Liebscher, A., Möller, F., Hennings, J., Kempka, T., Lüth, S., Norden, B., Prevedel, B., Szizybalski, A., Zimmer, M., Kühn, M., the Ketzin Group, 2013. CO₂ storage at the Ketzin pilot site, Germany: fourth year of injection, monitoring, modeling and verification. *Energy Proc.* 37, 6434–6443.
- Mikhailov, O.V., Queen, J., Toksöz, M.N., 2000. Using borehole electroseismic measurements to detect and characterize fractured (permeable) zones. *Geophysics* 65, 1098–1112.
- Moore, J., Glaser, S., Morrison, H., 2004. The streaming potential of liquid carbon dioxide in Berea sandstone. *Geophys. Res. Lett.* 31, L17610.
- Perrier, F., Morat, P., 2000. Characterization of electrical daily variations induced by capillary flow in the non-saturated zone. *Pure Appl. Geophys.* 157, 785–810.
- Pozzi, J.-P., Jouniaux, L., 1994. Electrical effects of fluid circulation in sediments and seismic prediction. *C.R. Acad. Sci. Paris* 318 (1), 73–77.
- Pride, S., 1994. Governing equations for the coupled electromagnetics and acoustics of porous media. *Phys. Rev. B: Condens. Matter* 50, 15678–15695.
- Pride, S., Garambois, S., 2005. Electrostatic wave theory of Frenkel and more recent developments. *J. Eng. Mech.*, 898–907.
- Pride, S., Haartsen, M.W., 1996. Electrostatic wave properties. *J. Acoust. Soc. Am.* 100, 1301–1315.
- Pride, S., Morgan, F.D., 1991. Electrokinetic dissipation induced by seismic waves. *Geophysics* 56 (7), 914–925.
- Pride, S.R., 2005. Relationships between Seismic and Hydrological Properties, vol. 50. Springer, The Netherlands <http://www.springerlink.com/content/h1167431tmm23135/abstract/>
- Reppert, P.M., Morgan, F.D., Lesmes, D.P., Jouniaux, L., 2001. Frequency-dependent streaming potentials. *J. Colloid Interface Sci.* 234, 194–203.
- Revil, A., Linde, N., Cerepi, A., Jougnot, D., Matthäi, S., Finsterle, S., 2007. Electrokinetic coupling in unsaturated porous media. *J. Colloid Interface Sci.* 313, 315–327.
- Ringrose, P., Atbi, M., Mason, D., Espinassous, M., Myhrer, O., Iding, M., Mathieson, A., Wright, I., 2009. Plume development around well KB-502 at the In Salah CO₂ storage site. *First Break* 27, 85–89.
- Santos, J., Ravazzoli, C., Gauzellino, P., Carcione, J., Cavallini, F., 2004. Simulation of waves in poro-viscoelastic rocks saturated by immiscible fluids. Numerical evidence of a second slow wave. *J. Comput. Acoust.* 12, 1–21.
- Schakel, M., Smeulders, D., Slob, E., Heller, H., 2011. Seismoelectric interface response: experimental results and forward model. *Geophysics* 76, N29–N36.
- Schakel, M., Smeulders, D., Slob, E., Heller, H., 2012. Seismoelectric fluid/porous-medium interface response model and measurements. *Transp. Porous Media* 93, 271–282.
- Schoemaker, F., Smeulders, D., Slob, E., 2007. Simultaneous determination of dynamic permeability and streaming potential. *SEG Expand. Abstr.* 26, 1555–1559.
- Strahser, M., Jouniaux, L., Sailhac, P., Matthey, P.-D., Zillmer, M., 2011. Dependence of seismoelectric amplitudes on water-content. *Geophys. J. Int.* 187, 1378–1392.
- Teja, A.S., Rice, P., 1981. Generalized corresponding states method for the viscosities of liquid mixtures. *Ind. Eng. Chem. Fund.* 20 (1), 77–81.
- Thibeau, S., Mucha, V., 2011. Have we overestimated saline aquifer CO₂ storage capacities? *Oil Gas Sci. Technol. Rev. IFP* 66 (1), 81–92.
- Thompson, A.H., Gist, G.A., 1993. Geophysical applications of electrokinetic conversion. *Lead. Edge* 12, 1169–1173.
- Vinogradov, J., Jaafar, M., Jackson, M.D., 2010. Measurement of streaming potential coupling coefficient in sandstones saturated with natural and artificial brines at high salinity. *J. Geophys. Res.* 115, B12204.
- Vinogradov, J., Jackson, M., 2011. Multiphase streaming potential in sandstones saturated with gas/brine and oil/brine during drainage and imbibition. *Geophys. Res. Lett.* 38, L01301.
- Wang, Z., Small, M., Karamalidis, A., 2013. Multimodel predictive system for carbon dioxide solubility in saline formation waters. *Environ. Sci. Technol.* 47, 1407–1415.
- Warden, S., Garambois, S., Jouniaux, L., Brito, D., Sailhac, P., Bordes, C., 2013. Seismoelectric wave propagation numerical modeling in partially saturated materials. *Geophys. J. Int.* 194, 1498–1513.
- Warden, S., Garambois, S., Sailhac, P., Jouniaux, L., Bano, M., 2012. Curvelet-based seismoelectric data processing. *Geophys. J. Int.* 190, 1533–1550.
- Wiese, B., Böhner, J., Enachescu, C., Würdemann, H., Zimmermann, G., 2010. Hydraulic characterisation of the Stuttgart formation at the pilot test site for CO₂ storage, Ketzin, Germany. *Int. J. Greenhouse Gas Control* 4, 960–971.
- Wiese, B., Zimmer, M., Nowak, M., Pellizzari, L., Pilz, P., 2013. Well-based hydraulic and geochemical monitoring of the above zone of the CO₂ reservoir at Ketzin, Germany. *Environ. Earth Sci.* 70, 3709–3726.
- Zhang, F., Juhlin, C., Cosma, C., Tryggvason, A., 2012. Cross-well seismic waveform tomography for monitoring CO₂ injection: a case study from the Ketzin site, Germany. *Geophys. J. Int.* 189, 629–646.
- Zhu, Z., Haartsen, M.W., Toksöz, M.N., 1999. Experimental studies of electrokinetic conversions in fluid-saturated borehole models. *Geophysics* 64, 1349–1356.
- Zyserman, F., Gauzellino, P., Santos, J., 2010. Finite element modeling of SHTE and PSVTM electroseismics. *J. Appl. Geophys.* 72, 79–91.
- Zyserman, F., Gauzellino, P., Santos, J., 2012. Numerical evidence of gas hydrate detection by means of electroseismics. *J. Appl. Geophys.* 86, 98–108.